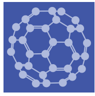 *nanomaterials*

MDPI

*Article*

# Effect of Device Scaling on Electron Mobility in Nanoscale GaN HEMTs with Polarization Charge Modulation

**Peng Cui [1,*] and Yuping Zeng [2,*]**

[1] Institute of Novel Semiconductors, Shandong University, Jinan 250100, China
[2] Department of Electrical and Computer Engineering, University of Delaware, Newark, DE 19716, USA
* Correspondence: pcui@sdu.edu.cn (P.C.); yzeng@udel.edu (Y.Z.)

**Abstract:** We have experimentally investigated the impact of vertical and lateral scaling on low-field electron mobility ($\mu$) in InAlN/GaN high-electron-mobility transistors (HEMTs). It is found that $\mu$ reduces as InAlN barrier ($T_B$) and gate length ($L_G$) scale down but increases with the scaled source–drain distance ($L_{SD}$). Polarization Coulomb Field (PCF) scattering is believed to account for the scaling-dependent electron mobility characteristic. The polarization charge distribution is modulated with the vertical and lateral scaling, resulting in the changes in $\mu$ limited by PCF scattering. The mobility characteristic shows that PCF scattering should be considered when devices scale down, which is significant for the device design and performance improvement for RF applications.

**Keywords:** GaN HEMTs; scaling; electron mobility; scattering; polarization charge

**Citation:** Cui, P.; Zeng, Y. Effect of Device Scaling on Electron Mobility in Nanoscale GaN HEMTs with Polarization Charge Modulation. *Nanomaterials* **2022**, *12*, 1718. https://doi.org/10.3390/nano12101718

Academic Editor: Antonio Di Bartolomeo

Received: 9 April 2022
Accepted: 12 May 2022
Published: 18 May 2022

**Publisher's Note:** MDPI stays neutral with regard to jurisdictional claims in published maps and institutional affiliations.

**Copyright:** © 2022 by the authors. Licensee MDPI, Basel, Switzerland. This article is an open access article distributed under the terms and conditions of the Creative Commons Attribution (CC BY) license (https://creativecommons.org/licenses/by/4.0/).

## 1. Introduction

Due to the high breakdown voltage, high two-dimensional electron gas densities, and high electron saturation velocity, gallium nitride (GaN) high-electron-mobility transistors (HEMTs) have been ideal for high-frequency and high-power applications, such as radar communications, electronic countermeasures, 5G applications, small base stations, new communication microsatellites, power transmission and automotive electronics [1–5]. Yan Tang et al. fabricated the AlN/GaN/AlGaN double heterojunction HEMTs with fully passivation and $n^+$-GaN ohmic contact regrowth technology, demonstrating a record high current/power gain cutoff frequency $f_T/f_{max}$ of 454/444 GHz on a 20 nm-gate-length HEMT with gate–source and gate–drain spacings of 50 nm [6]. Jeong-Gil Kim et al. reported an AlGaN/GaN HEMT structure on the high-quality undoped thick AlN buffer layer with a high breakdown voltage of 2154 V and a very high figure of merit (FOM) of ~1.8 $GV^2 \cdot \Omega^{-1} \cdot cm^{-2}$ [7]. Xiaoyu Xia et al. reported a new type of AlGaN/GaN HEMTs with a microfield plate (FP) with a breakdown voltage increase from 870 V to 1278 V by adjusting the distribution of the potential and channel electric field [8]. Maddaka Reddeppa et al. demonstrated high photoresponse and the electrical transport properties of a pristine GaN nanorod-based Schottky diode with an optimized Schottky barrier height [9]. Kedhareswara Sairam Pasupuleti et al. developed the integration of conductive polypyrrole (Ppy) and GaN nanorods for high-performance self-powered UV-A photodetectors, exhibiting superior photoresponse properties such as detectivity, responsivity, external quantum efficiency, good stability and reproducibility [10].

To further improve device performance, device scaling in GaN HEMTs is necessary [6,11,12]. The effects of scaling on short-channel effects (SECs), leakage current, electron velocity, frequency characteristics have been studied [13–18], providing insightful guidance for device design and performance improvement. However, few studies about the impact of scaling on electron mobility have been reported. In general, low-field mobility should not change when devices scale down. However, due to the spontaneous and piezoelectric polarization in GaN HEMTs, there are polarization charges in the barrier layer [19,20], which

is different from conventional transistors (Si, GaAs, et al.). The change in the polarization charge distribution is related to the device dimension and can result in scattering on the channel electrons [21,22], which leads to a possible change in mobility with device scaling. In this article, to demonstrate this influence, the InAlN/GaN HEMTs with various barrier thicknesses, source–drain distances, and gate lengths are fabricated and the effect of scaling on electron mobility is studied.

## 2. Experiment

The lattice-matched $In_{0.17}Al_{0.83}N$/GaN HEMT structure is grown by metal–organic chemical vapor deposition on a Si substrate, as shown in Figure 1, consisting of a 2 nm GaN cap, an InAlN barrier, a 1 nm AlN interlayer, a 15 nm GaN channel layer, a 4 nm $In_{0.12}Ga_{0.88}N$ back-barrier and a 2 µm undoped GaN buffer. Here, two different InAlN layers with the thicknesses of 8 nm and 5 nm are grown. The device process started with mesa isolation with $Cl_2$-based inductively coupled plasma (ICP) etching. Then, Ohmic contact was formed with Ti/Al/Ni/Au metal deposition and annealed at 850 °C for 40 s. Ni/Au gate Schottky contact was deposited in the center of the source–drain region to complete the process. For the large devices, the gate length ($L_G$), gate–source distance ($L_{GS}$), and gate–drain distance ($L_{GD}$) of the devices are all 2 µm. For the RF devices, two types of devices are fabricated. For type I, $L_G$ of the devices is fixed at 50 nm and $L_{SD}$ is 2, 1, and 0.6 µm, respectively. For type II, $L_{SD}$ of the devices is fixed at 1 µm and $L_G$ is 50, 100, and 150 nm, respectively. Here, the gate of all the devices is located between the source and drain regions, and the gate width is 2 × 20 µm. The current–voltage ($I$–$V$) and capacitance–voltage ($C$–$V$) measurements were carried out by using an Agilent B1500A semiconductor parameter analyzer (Agilent Technologies, Santa Clara, CA, USA).

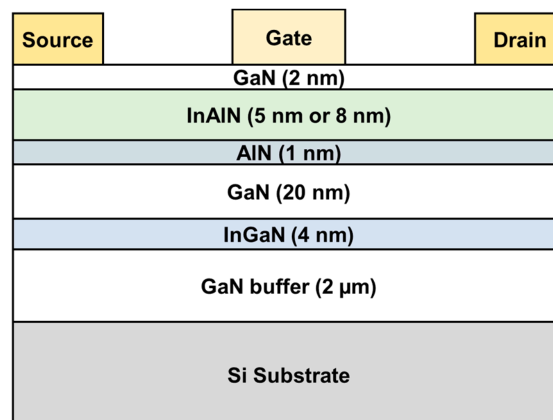


**Figure 1.** Schematic cross-section of the fabricated InAlN/GaN HEMT with two different InAlN barrier thickness (8 nm and 5 nm, respectively).

## 3. Results and Discussion

Figure 2a,b show the measured capacitances ($C$) of the InAlN/GaN circle diodes with both InAlN barrier thicknesses ($T_B$). Here, six devices are measured and a good consistency is presented. An improved $C$ and a subthreshold voltage ($V_T$) shift are observed due to the reduced InAlN barrier thickness ($C = \varepsilon/T_B$, $\varepsilon$ is the dielectric constant of InAlN barrier). Through integrating C-V curves, electron density ($n_{2D}$) is extracted as shown in Figure 2c,d. It shows that the InAlN/GaN heterostructure with 8 nm InAlN barrier presents higher electron density. Figure 3 shows the simulated band structure and 2DEG electron density as a function of the distance from the material surface of the InAlN/GaN heterostructure, which is calculated by self-consistently solving Schrodinger's and Poisson's equations [23,24]. Compared with the 5 nm InAlN barrier, the InAlN/GaN heterostructure with an 8 nm InAlN barrier also shows a higher electron density peak. In GaN HEMTs, the surface states are identified as the source of channel electrons. Due to the spontaneous

polarization filed, the increase in InAlN barrier thickness can increase the energy of the surface states, resulting in higher electron density [25,26].

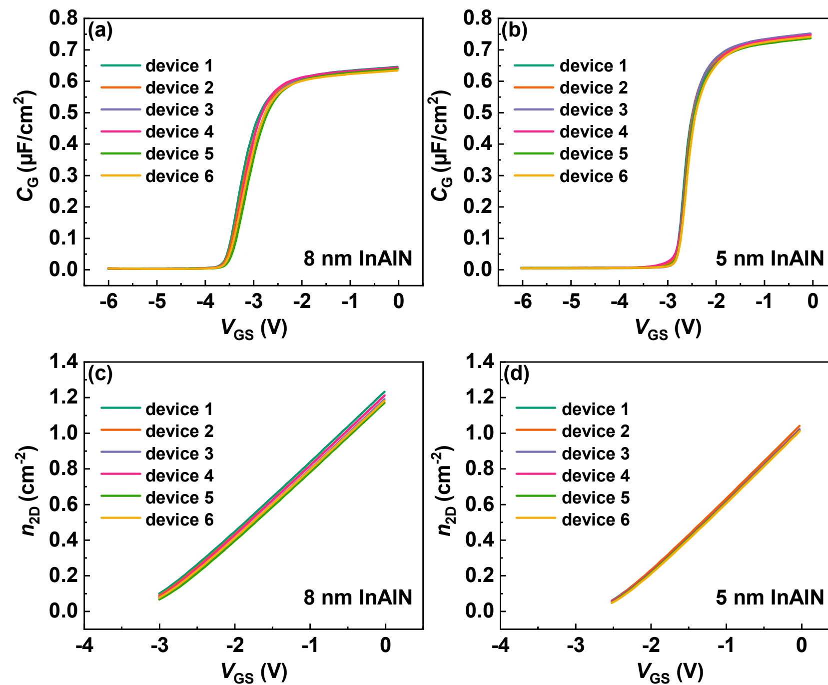


**Figure 2.** Gate capacitance ($C_G$) of the InAlN/GaN diode with (**a**) 8 nm InAlN and (**b**) 5 nm InAlN, respectively. Two-dimensional electron gas electron density ($n_{2D}$) of the InAlN/GaN diode with (**c**) 8 nm InAlN and (**d**) 5 nm InAlN, respectively.

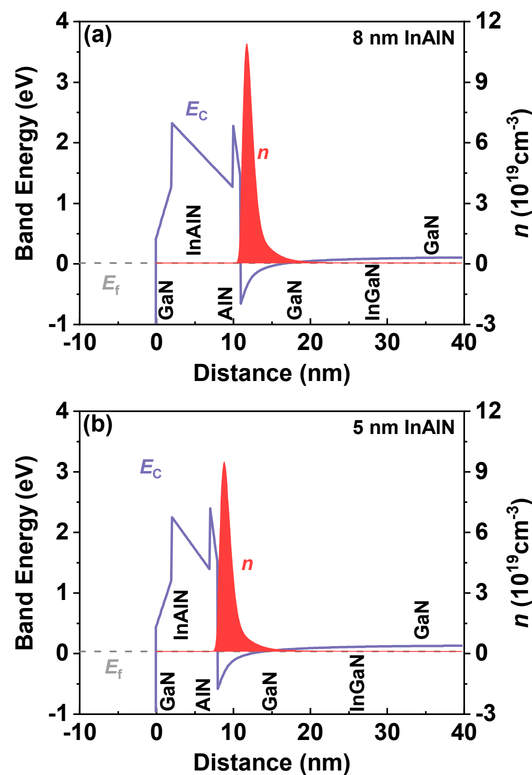


**Figure 3.** Simulated band structure and 2DEG electron density as a function of the distance from the material surface of the InAlN/GaN heterostructure with (**a**) 8 nm InAlN and (**b**) 5 nm InAlN, respectively.

Figure 4 shows the output characteristics of the InAlN/GaN HEMTs with different InAlN thickness. The $L_G$, $L_{GS}$, and $L_{GD}$ of the devices are all 2 μm. To extract low-field mobility, the drain current ($I_D$) at $V_{DS}$ = 0.1 V in the output characteristics are used. At $V_{GS}$ = 0 V, the total source–drain resistance ($R_{SD}$) can be written as

$$R_{SD} = \frac{V_{DS}}{I_{DS}} = 2R_C + \frac{L_G + L_{GS} + L_{GD}}{n_{2D0} q \mu_0} \tag{1}$$

where $R_C$ is the ohmic contact resistance, $q$ is the electron charge, and $\mu_0$ and $n_{2D0}$ are the electron mobility and electron density under the gate region with $V_{GS}$ = 0 V. Here, only $\mu_0$ and $R_C$ are unknown. Electron mobility in GaN HEMTs is limited by polar optical phonon ($\mu_{POP}$), polarization Coulomb field ($\mu_{PCF}$), acoustic phonon ($\mu_{AP}$), interface roughness ($\mu_{IFR}$), and dislocation ($\mu_{DIS}$) scatterings [22,27,28]. PCF scattering is related to the nonuniformity of polarization charge distribution [21,22]. At $V_{GS}$ = 0 V, the polarization charge distribution is uniform, and the PCF can be neglected. Based on the two-dimensional (2D) scattering theory and the obtained $n_{2D0}$ [27], $\mu_0$ can be calculated with $1/\mu_0 = 1/\mu_{POP} + 1/\mu_{AP} + 1/\mu_{IFR} + 1/\mu_{DIS}$, and then $R_C$ can be determined with (1). Based on the obtained $n_{2D0}$ and $\mu_0$, the electron mobility $\mu$ under the gate region under different $V_{GS}$ can be extracted from

$$\frac{V_{DS}}{I_{DS}} = 2R_C + \frac{L_G}{n_{2D} q \mu} + \frac{L_{GS} + L_{GD}}{n_{2D0} q \mu_0} \tag{2}$$

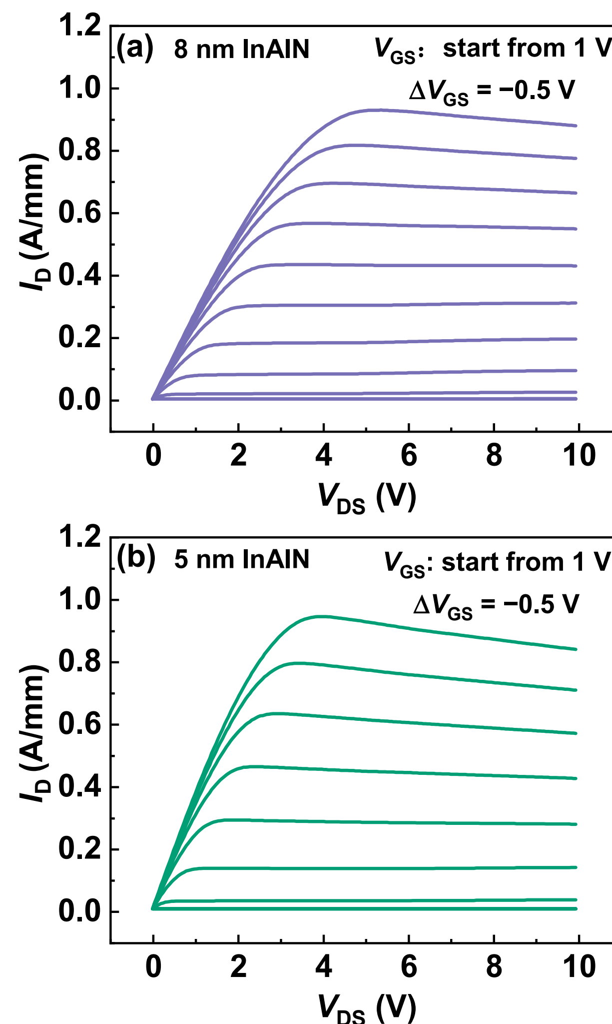


**Figure 4.** Output characteristics of the InAlN/GaN HEMTs with (**a**) 8 nm InAlN and (**b**) 5 nm InAlN, respectively.

Figure 5 depicts the extracted $\mu$ versus $V_{GS}$ for both samples. At $V_{GS}$ = 0 V, $\mu$ of the devices with 8 nm InAlN and 5 nm InAlN is 1221 and 1651 $cm^2/V{\cdot}s$, respectively. The improved electron mobility with a thinner barrier is also confirmed with the Hall measurement (1242 $cm^2/V{\cdot}s$ for 8 nm InAlN and 1663 $cm^2/V{\cdot}s$ for 5 nm InAlN) and the electron mobility of Fat-FETs (with $L_G$ of 96 µm and $L_{SD}$ of 100 µm, 1101 $cm^2/V{\cdot}s$ for 8 nm InAlN and 1670 $cm^2/V{\cdot}s$ for 5 nm InAlN) [29].

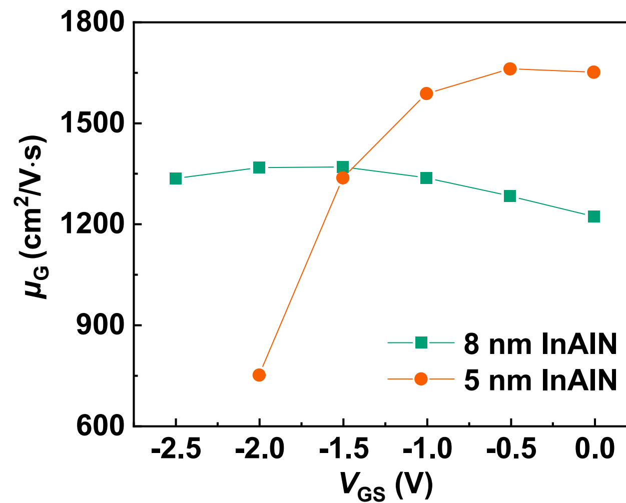


**Figure 5.** Extracted $\mu$ versus $V_{GS}$ of the devices with 8 nm and 5 nm InAlN.

As shown in Figure 5, $\mu$ presents a different trend versus $V_{GS}$ for the devices with different InAlN thickness. As $V_{GS}$ increases, $\mu$ of the device with 8 nm InAlN deceases, but that of the device with 5 nm InAlN increases. Figure 6a,b show the calculated $\mu$ limited by different scatterings for both devices [21,30,31]. The calculated $\mu$ ($\mu_{CAL}$, lines in the figures) by using 2D scattering theory shows good agreement with the extracted $\mu$ (scatters in the figures), which proves the accuracy of the calculation. As $V_{GS}$ increases, $\mu_{POP}$ and $\mu_{IFR}$ decrease, $\mu_{DIS}$ and $\mu_{PCF}$ increase, and $\mu_{AP}$ presents a slight change. $\mu_{POP}$ and $\mu_{PCF}$ play more significant roles among all the scatterings. Figure 7 compares $\mu_{POP}$ and $\mu_{PCF}$ for both devices. When the InAlN barrier decreases from 8 nm to 5 nm, $\mu_{POP}$ increases while $\mu_{PCF}$ decreases. The reduced $n_{2D}$ with a 5 nm InAlN barrier decreases the collision probability between channel electrons and polar optical phonons (POPs), resulting in the improved $\mu_{POP}$ [27,28]. Due to the spontaneous polarization, there are polarization charges ($\rho_0$) in the InAlN barrier near the InAlN/GaN interface. When $V_{GS}$ is applied on the gate terminal, the polarization charges ($\rho_G$) under the gate region are changed due to the inverse piezoelectric effect [32], as shown in Figure 8. The polarization charge distribution is not uniform, and the potential periodicity is broken, resulting in polarization Coulomb field (PCF) scattering. The PCF scattering potential is from the additional polarization charges ($\sigma = \rho_0 - \rho_G$) and is written as [21,22]

$$\begin{aligned} V(x,y,z) = \; & -\frac{q}{4\pi\varepsilon}\int_{-L_{GS}-\frac{L_G}{2}}^{\frac{L_G}{2}} dx' \int_0^{W_G} \frac{\sigma}{\sqrt{(x-x')^2+(y-y')^2+z^2}} dy' \\ & -\frac{q}{4\pi\varepsilon}\int_{\frac{L_G}{2}}^{\frac{L_{GD}}{2}+\frac{L_G}{2}} dx' \int_0^{W_G} \frac{\sigma}{\sqrt{(x-x')^2+(y-y')^2+z^2}} dy' \end{aligned} \quad (3)$$

where $\varepsilon$ is the dielectric constant of GaN and $W_G$ is the gate width. Based on inverse piezoelectric effect, $\sigma$ can be calculated by using $\sigma = \rho_0 - \rho_G = -ne_{33}{}^2V_{GS}/(C_{33}d)$ [32]. $n$ is the fitting parameter, and $e_{33}$ and $C_{33}$ are the piezoelectric coefficient and the elastic stiffness tensor of InAlN, respectively. $d$ is the gate-to-channel distance, which is the sum of the thicknesses of the GaN cap layer (2 nm), InAlN barrier (8 or 5 nm), and AlN interlayer (1 nm). Figure 9 depicts the calculated $\sigma$ versus $V_{GS}$ with an 8 and 5 nm InAlN barrier. $\sigma$ increases with the decreased $T_B$ and $V_{GS}$, resulting in the enhanced PCF scattering as the

InAlN barrier thickness and $V_{GS}$ decrease. Therefore, $\mu_{PCF}$ increases with $V_{GS}$. Because the device with a 5 nm InAlN barrier shows an enhanced PCF scattering, $\mu$ increases with $V_{GS}$. This fact is more pronounced, especially in the more negative $V_{GS}$ region. For the device with an 8 nm InAlN barrier, the PCF scattering became weaker and the POP scattering dominates $\mu$, leading to a slight decrease in $\mu$ when $V_{GS}$ increases.

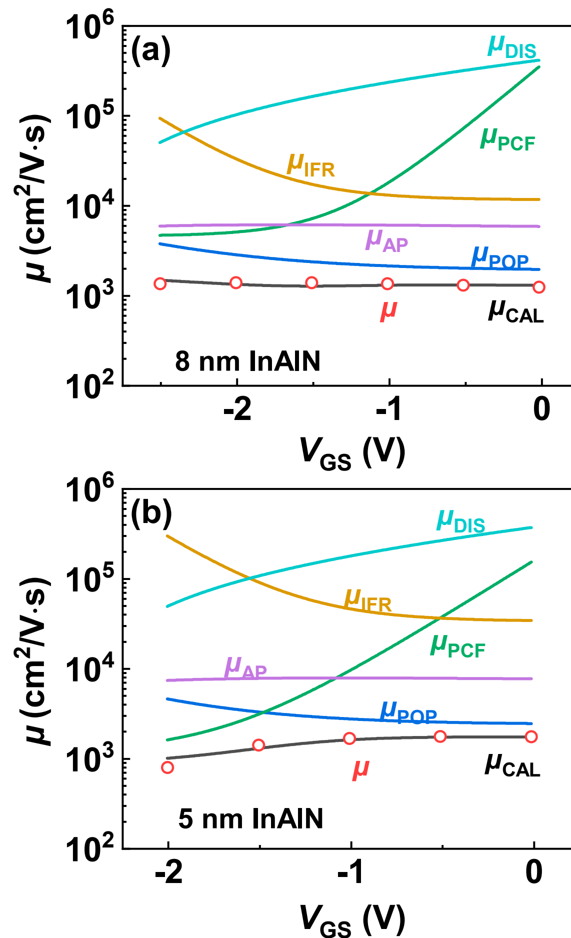


**Figure 6.** (**a**,**b**) Calculated $\mu$ limited by different scattering mechanisms, extracted $\mu$ ($\mu$, scatters), and calculated $\mu$ ($\mu_{CAL}$, lines) versus $V_{GS}$ of both samples.

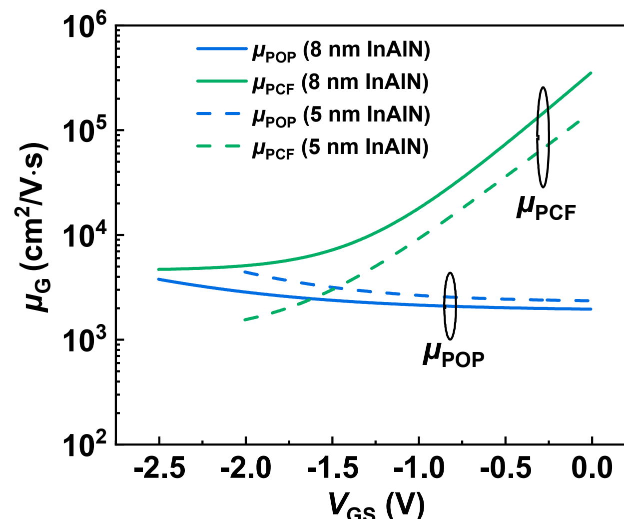


**Figure 7.** Comparison of $\mu_{POP}$ and $\mu_{PCF}$ versus $V_{GS}$ of both samples.

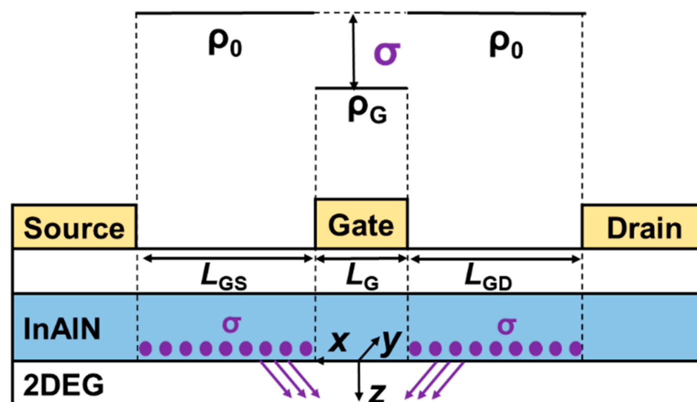


**Figure 8.** Schematic of the additional polarization charge (σ) distribution in InAlN barrier.

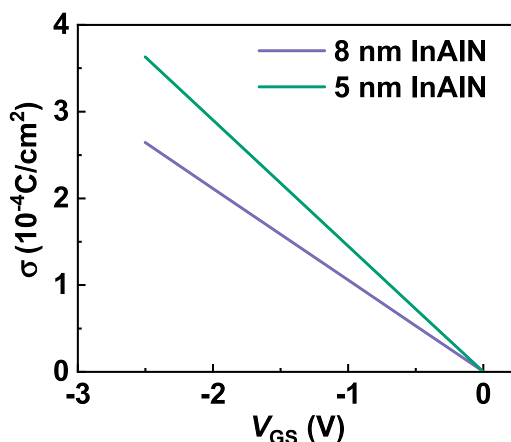


**Figure 9.** Additional polarization charge (σ) versus $V_{GS}$ with 8 nm and 5 nm InAlN barrier.

From the above discussions, the vertical scale will increase σ and thus enhance PCF scattering, leading to a reduced $\mu$. The lateral scaling is also experimentally investigated on the devices by varying $L_{SD}$ and $L_G$ using the same electron mobility extraction methodology. As the device laterally scales, $n_{2D}$ is not changed, so POP, AP, IFR, and DIS scatterings are not affected. Only PCF scattering can be changed due to the modulation of the polarization change distribution. Figure 10a,b present $\mu$ versus $V_{GS}$ at $V_{DS}$ = 0.1 V for the devices with $L_G$ of 50 nm and $L_{SD}$ of 2, 1, 0.6 µm with 8 nm and 5 nm InAlN. $\mu$ presents an increase with the decrease in $L_{SD}$. The corresponding $\mu_{PCF}$ is also calculated and plotted in Figure 10c,d. As shown in Figure 11a,b, as $L_{SD}$ scales down, the number of σ is reduced and the effect of σ on the electron under the gate region is weakened, resulting in the increased $\mu_{PCF}$ and $\mu$. Because PCF scattering in the device with 8 nm InAlN is weaker, the increase in $\mu$ due to the downscaling of $L_{SD}$ is more significant. Here, $\mu$ of the devices with $L_G$ of 2 µm is also plotted for comparison, and a significant decrease in $\mu$ in the device with an $L_G$ of 50 nm is observed. Although the number of σ is the same under the same $V_{GS}$, the effect of σ on the 50 nm gate is stronger and thus PCF scattering is enhanced, leading to a decreased $\mu$.

Figure 12a,b present the $\mu$ versus $V_{GS}$ for the devices with $L_{SD}$ of 1 µm and $L_G$ of 50, 100, 150 nm with 8 nm and 5 nm InAlN. The electron mobility of all devices presents an increase with $V_{GS}$. This means PCF scattering plays a dominant role in the electron mobility. As $V_{GS}$ increases from a negative value to 0 V, the electric field under the gate region decreases, resulting in the increase in $\mu_{PCF}$ and $\mu$. For the devices with different gate lengths, $\mu$ presents an increase as $L_G$ increases. This means the increase in gate length can increase the electron mobility. To explain this phenomenon, the corresponding $\mu_{PCF}$ is calculated and plotted in Figure 12c,d. It shows that the increase in $L_G$ can weaken PCF scattering and increase $\mu_{PCF}$. Because $L_{SD}$ is fixed, as shown in Figure 13, the decreased $L_G$ means the increased $L_{GS}$ and $L_{GD}$, resulting in the enhanced effect of σ on the electrons

under the gate region. Thus, PCF scattering becomes stronger and $\mu$ reduces with the downscaled $L_G$.

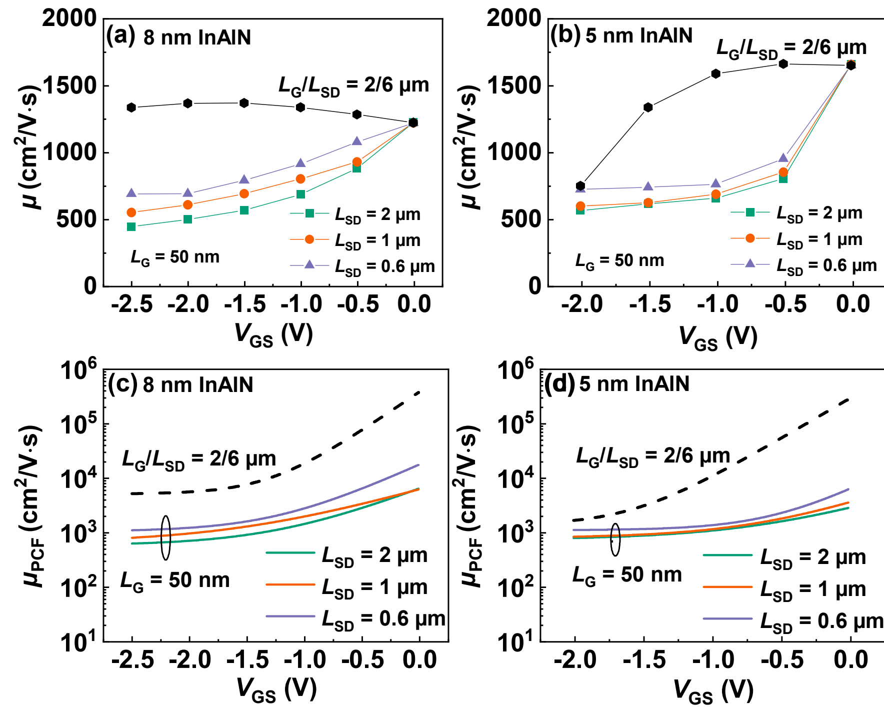


**Figure 10.** $\mu$ versus $V_{GS}$ for the devices with $L_G$ of 50 nm and $L_{SD}$ of 2, 1, 0.6 μm with (**a**) 8 nm and (**b**) 5 nm InAlN. The device with $L_G/L_{SD}$ of 2/6 μm is also plotted for comparison. Calculated $\mu_{PCF}$ versus $V_{GS}$ of the same devices with (**c**) 8 nm and (**d**) 5 nm InAlN. The device with $L_G/L_{SD}$ of 2/6 μm is also plotted for comparison.

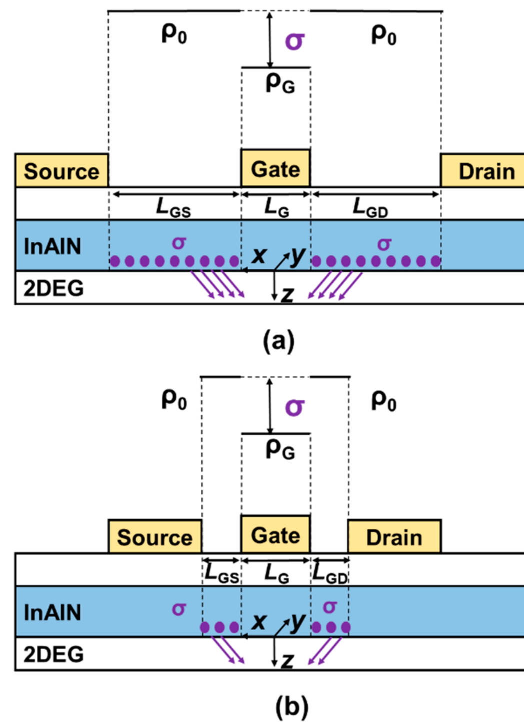


**Figure 11.** Schematic of the additional polarization charge (σ) distribution in InAlN barrier with (**a**) large and (**b**) small source–drain spacing $L_{SD}$. The gate length is fixed.

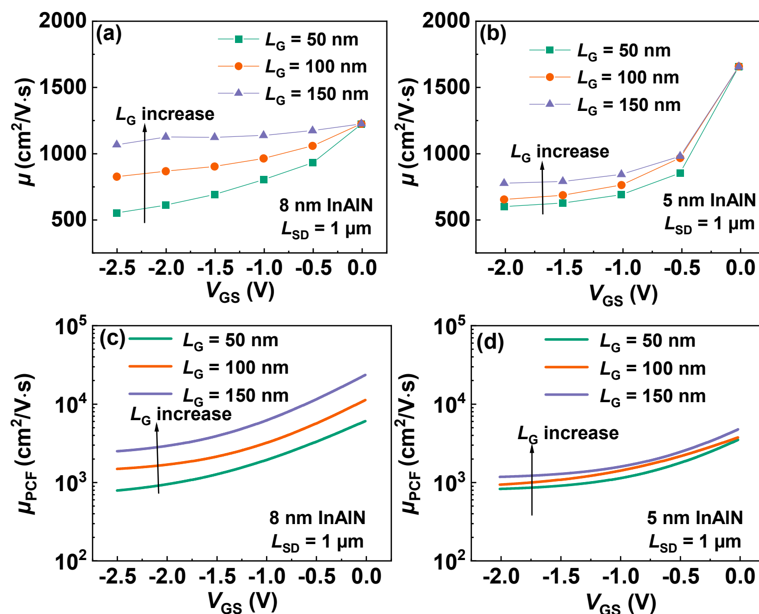


**Figure 12.** (**a**,**b**) $\mu$ versus $V_{GS}$ for the devices with $L_{SD}$ of 1 μm and $L_G$ of 50, 100, 150 nm with 8 nm and 5 nm InAlN. (**c**,**d**) Calculated $\mu_{PCF}$ versus $V_{GS}$ of the same devices with 8 nm and 5 nm InAlN.

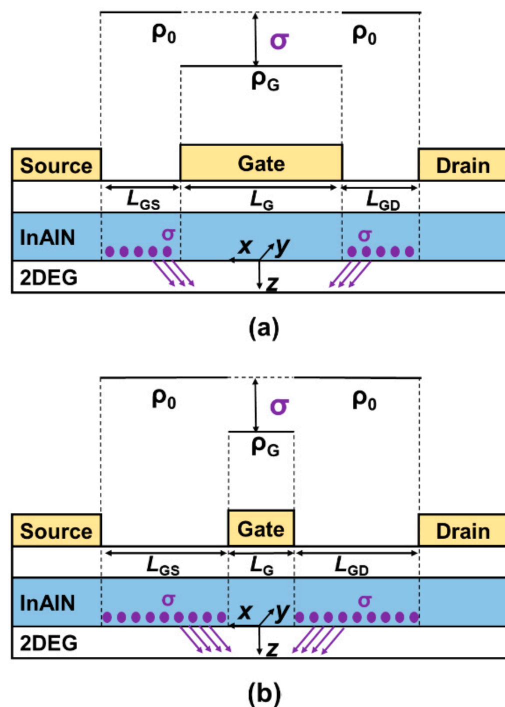


**Figure 13.** Schematic of the additional polarization charge (σ) distribution in InAlN barrier with (**a**) large and (**b**) small gate length $L_G$. The source–drain spacing $L_{SD}$ is fixed.

## 4. Conclusions

In summary, the effect of down-scaling on electron mobility is experimentally demonstrated. It shows that the downscaling of barrier thickness and $L_G$ results in a decrease in $\mu$, but downscaled $L_{SD}$ leads to an increase in $\mu$. This is because the polarization charge distribution is modulated with the vertical and lateral scale, resulting in a change in PCF scattering. When GaN HEMTs scale down, the effect of PCF scattering should be considered, providing an insightful guidance for the device geometry design and performance improvement for RF application.

**Author Contributions:** P.C. and Y.Z. contributed to the research design, experiment measurements, data analysis, and manuscript preparation. All authors have read and agreed to the published version of the manuscript.

**Funding:** This research was funded in part by the NASA International Space Station under Grant 80NSSC20M0142, and in part by Air Force Office of Scientific Research under Grant FA9550-19-1-0297, Grant FA9550-21-1-0076 and Grant FA9550-22-1-0126.

**Institutional Review Board Statement:** Not applicable.

**Informed Consent Statement:** Not applicable.

**Data Availability Statement:** The data presented in this study are available upon request from the corresponding author.

**Conflicts of Interest:** The authors declare no conflict of interest.

## References

1. Hamza, K.H.; Nirmal, D. A review of GaN HEMT broadband power amplifiers. *AEU—Int. J. Electron. Commun.* **2020**, *116*, 153040. [CrossRef]
2. Ma, C.-T.; Gu, Z.-H. Review of GaN HEMT applications in power converters over 500 W. *Electronics* **2019**, *8*, 1401. [CrossRef]
3. Keshmiri, N.; Wang, D.; Agrawal, B.; Hou, R.; Emadi, A. Current status and future trends of GaN HEMTs in electrified transportation. *IEEE Access* **2020**, *8*, 70553–70571. [CrossRef]
4. Li, L.; Nomoto, K.; Pan, M.; Li, W.; Hickman, A.; Miller, J.; Lee, K.; Hu, Z.; Bader, S.J.; Lee, S.M. GaN HEMTs on Si with regrown contacts and cutoff/maximum oscillation frequencies of 250/204 GHz. *IEEE Electron Device Lett.* **2020**, *41*, 689–692. [CrossRef]
5. Cui, P.; Mercante, A.; Lin, G.; Zhang, J.; Yao, P.; Prather, D.W.; Zeng, Y. High-performance InAlN/GaN HEMTs on silicon substrate with high fT× Lg. *Appl. Phys. Express* **2019**, *12*, 104001. [CrossRef]
6. Tang, Y.; Shinohara, K.; Regan, D.; Corrion, A.; Brown, D.; Wong, J.; Schmitz, A.; Fung, H.; Kim, S.; Micovic, M. Ultrahigh-Speed GaN High-Electron-Mobility Transistors With $f_T/f_{max}$ of 454/444 GHz. *IEEE Electron Device Lett.* **2015**, *36*, 549–551. [CrossRef]
7. Kim, J.-G.; Cho, C.; Kim, E.; Hwang, J.S.; Park, K.-H.; Lee, J.-H. High breakdown voltage and low-current dispersion in AlGaN/GaN HEMTs with high-quality AlN buffer layer. *IEEE Trans. Electron Devices* **2021**, *68*, 1513–1517. [CrossRef]
8. Xia, X.; Guo, Z.; Sun, H. Study of Normally-Off AlGaN/GaN HEMT with Microfield Plate for Improvement of Breakdown Voltage. *Micromachines* **2021**, *12*, 1318. [CrossRef]
9. Reddeppa, M.; Park, B.-G.; Pasupuleti, K.S.; Nam, D.-J.; Kim, S.-G.; Oh, J.-E.; Kim, M.-D. Current–voltage characteristics and deep-level study of GaN nanorod Schottky-diode-based photodetector. *Semicond. Sci. Technol.* **2021**, *36*, 035010. [CrossRef]
10. Pasupuleti, K.S.; Reddeppa, M.; Park, B.-G.; Oh, J.-E.; Kim, S.-G.; Kim, M.-D. Efficient Charge Separation in Polypyrrole/GaN-Nanorod-Based Hybrid Heterojunctions for High-Performance Self-Powered UV Photodetection. *Phys. Status Solidi (RRL)—Rapid Res. Lett.* **2021**, *15*, 2000518. [CrossRef]
11. Schuette, M.L.; Ketterson, A.; Song, B.; Beam, E.; Chou, T.-M.; Pilla, M.; Tserng, H.-Q.; Gao, X.; Guo, S.; Fay, P.J. Gate-recessed integrated E/D GaN HEMT technology with $f_T/f_{max}$ > 300 GHz. *IEEE Electron Device Lett.* **2013**, *34*, 741–743. [CrossRef]
12. Downey, B.P.; Meyer, D.J.; Katzer, D.S.; Roussos, J.A.; Pan, M.; Gao, X. $SiN_x$/InAlN/AlN/GaN MIS-HEMTs With 10.8 THz·V Johnson Figure of Merit. *IEEE Electron Device Lett.* **2014**, *35*, 527–529. [CrossRef]
13. Jessen, G.H.; Fitch, R.C.; Gillespie, J.K.; Via, G.; Crespo, A.; Langley, D.; Denninghoff, D.J.; Trejo, M.; Heller, E.R. Short-channel effect limitations on high-frequency operation of AlGaN/GaN HEMTs for T-Gate devices. *IEEE Trans. Electron Devices* **2007**, *54*, 2589–2597. [CrossRef]
14. Shinohara, K.; Regan, D.C.; Tang, Y.; Corrion, A.L.; Brown, D.F.; Wong, J.C.; Robinson, J.F.; Fung, H.H.; Schmitz, A.; Oh, T.C. Scaling of GaN HEMTs and Schottky diodes for submillimeter-wave MMIC applications. *IEEE Trans. Electron Devices* **2013**, *60*, 2982–2996. [CrossRef]
15. Shinohara, K.; Regan, D.; Milosavljevic, I.; Corrion, A.; Brown, D.; Willadsen, P.; Butler, C.; Schmitz, A.; Kim, S.; Lee, V. Electron velocity enhancement in laterally scaled GaN DH-HEMTs with $f_T$ of 260 GHz. *IEEE Electron Device Lett.* **2011**, *32*, 1074–1076. [CrossRef]
16. Shinohara, K.; Regan, D.; Corrion, A.; Brown, D.; Burnham, S.; Willadsen, P.; Alvarado-Rodriguez, I.; Cunningham, M.; Butler, C.; Schmitz, A. Deeply-scaled self-aligned-gate GaN DH-HEMTs with ultrahigh cutoff frequency. In Proceedings of the 2011 International Electron Devices Meeting, Washington, DC, USA, 5–7 December 2011; pp. 11–14.
17. Medjdoub, F.; Alomari, M.; Carlin, J.-F.; Gonschorek, M.; Feltin, E.; Py, M.; Grandjean, N.; Kohn, E. Barrier-layer scaling of InAlN/GaN HEMTs. *IEEE Electron Device Lett.* **2008**, *29*, 422–425. [CrossRef]
18. Lee, D.S.; Lu, B.; Azize, M.; Gao, X.; Guo, S.; Kopp, D.; Fay, P.; Palacios, T. Impact of GaN channel scaling in InAlN/GaN HEMTs. In Proceedings of the 2011 International Electron Devices Meeting, Washington, DC, USA, 5–7 December 2011; pp. 11–14.
19. Ambacher, O.; Foutz, B.; Smart, J.; Shealy, J.; Weimann, N.; Chu, K.; Murphy, M.; Sierakowski, A.; Schaff, W.; Eastman, L. Two dimensional electron gases induced by spontaneous and piezoelectric polarization in undoped and doped AlGaN/GaN heterostructures. *J. Appl. Phys.* **2000**, *87*, 334–344. [CrossRef]

20. Yu, E.; Sullivan, G.; Asbeck, P.; Wang, C.; Qiao, D.; Lau, S. Measurement of piezoelectrically induced charge in GaN/AlGaN heterostructure field-effect transistors. *Appl. Phys. Lett.* **1997**, *71*, 2794–2796. [CrossRef]
21. Luan, C.; Lin, Z.; Lv, Y.; Zhao, J.; Wang, Y.; Chen, H.; Wang, Z. Theoretical model of the polarization Coulomb field scattering in strained AlGaN/AlN/GaN heterostructure field-effect transistors. *J. Appl. Phys.* **2014**, *116*, 044507. [CrossRef]
22. Cui, P.; Mo, J.; Fu, C.; Lv, Y.; Liu, H.; Cheng, A.; Luan, C.; Zhou, Y.; Dai, G.; Lin, Z. Effect of Different Gate Lengths on Polarization Coulomb Field Scattering Potential in AlGaN/GaN Heterostructure Field-Effect Transistors. *Sci. Rep.* **2018**, *8*, 9036. [CrossRef]
23. Lin, Z.; Zhao, J.; Corrigan, T.D.; Wang, Z.; You, Z.; Wang, Z.; Lu, W. The influence of Schottky contact metals on the strain of AlGaN barrier layers. *J. Appl. Phys.* **2008**, *103*, 044503. [CrossRef]
24. Guo, L.; Wang, X.; Wang, C.; Xiao, H.; Ran, J.; Luo, W.; Wang, X.; Wang, B.; Fang, C.; Hu, G. The influence of 1 nm AlN interlayer on properties of the $Al_{0.3}Ga_{0.7}N$/AlN/GaN HEMT structure. *Microelectron. J.* **2008**, *39*, 777–781. [CrossRef]
25. Ibbetson, J.P.; Fini, P.; Ness, K.; DenBaars, S.; Speck, J.; Mishra, U. Polarization effects, surface states, and the source of electrons in AlGaN/GaN heterostructure field effect transistors. *Appl. Phys. Lett.* **2000**, *77*, 250–252. [CrossRef]
26. Goyal, N.; Fjeldly, T.A. Analytical modeling of AlGaN/AlN/GaN heterostructures including effects of distributed surface donor states. *Appl. Phys. Lett.* **2014**, *105*, 023508. [CrossRef]
27. Gurusinghe, M.; Davidsson, S.; Andersson, T. Two-dimensional electron mobility limitation mechanisms in $Al_xGa_{1-x}N$/GaN heterostructures. *Phys. Rev. B* **2005**, *72*, 045316. [CrossRef]
28. Fang, T.; Wang, R.; Xing, H.; Rajan, S.; Jena, D. Effect of optical phonon scattering on the performance of GaN transistors. *IEEE Electron Device Lett.* **2012**, *33*, 709–711. [CrossRef]
29. Kordoš, P.; Gregušová, D.; Stoklas, R.; Čičo, K.; Novák, J. Improved transport properties of $Al_2O_3$/AlGaN/GaN metal-oxide-semiconductor heterostructure field-effect transistor. *Appl. Phys. Lett.* **2007**, *90*, 123513. [CrossRef]
30. Cui, P.; Lv, Y.; Fu, C.; Liu, H.; Cheng, A.; Luan, C.; Zhou, Y.; Lin, Z. Effect of Polarization Coulomb Field Scattering on Electrical Properties of the 70-nm Gate-Length AlGaN/GaN HEMTs. *Sci. Rep.* **2018**, *8*, 12850. [CrossRef]
31. Cui, P.; Liu, H.; Lin, W.; Lin, Z.; Cheng, A.; Yang, M.; Liu, Y.; Fu, C.; Lv, Y.; Luan, C. Influence of different gate biases and gate lengths on parasitic source access resistance in AlGaN/GaN heterostructure FETs. *IEEE Trans. Electron Devices* **2017**, *64*, 1038–1044. [CrossRef]
32. Anwar, A.; Webster, R.T.; Smith, K.V. Bias induced strain in AlGaN/GaN heterojunction field effect transistors and its implications. *Appl. Phys. Lett.* **2006**, *88*, 203510. [CrossRef]